PNAS RESEARCH ARTICLE | APPLIED PHYSICAL SCIENCES

Chirality-induced phonon spin selectivity by elastic spin–orbit interaction

Chenwen Yang[a] and Jie Ren[a,1]

Affiliations are included on p. 8.

Edited by Guancong Ma, Hong Kong Baptist University, Kowloon Tong, Hong Kong; received June 7, 2024; accepted September 30, 2024 by Editorial Board Member John A. Rogers

Spin and orbital degrees of freedom are crucial in not only fundamental particles but also classical waves such as optical systems, wherein the spin–orbit interaction (SOI) of light provides new perspectives for manipulating electromagnetic waves. Elastic waves possess similar spin angular momentum (SAM) and orbital angular momentum (OAM). However, the elastic counterpart of SOI remains unexplored, even for ubiquitous elastic waveguides (WG). Here, we demonstrate the existence of elastic SOI in helical WG. We prove that the torsion and curvature of helical WG induces synthetic gauge potentials in describing the elastic vibrations. Through analytical theory and simulations, we unveil the interplay among elastic SAM, intrinsic OAM, and extrinsic OAM, impacted by the elastic SOI. Importantly, results show that elastic SOI can introduce the Chirality-Induced Phonon Spin Selectivity. These findings advance our understanding of angular momentum physics in elastic waves and enable practical strategies for wave manipulation.

spin–orbit interaction | elastic spin | phonon spin

Significance

The study of vector waves involves the spin–orbit interaction, which is fundamental to phenomena such as the spin–Hall effect of light and plays a crucial role in wave manipulation. In this research, we have revealed the spin–orbit interaction of elastic waves and elucidated the associated angular momentum structure. Importantly, our findings demonstrate that the spin–orbit interaction of elastic waves can lead to Chirality-Induced Phonon Spin Selectivity. The results show that elastic waveguides can selectively transport signals with phonon spin based on the chirality of structure. Considering the pivotal role of elastic spin–orbit interaction as fundamental ingredient in phononic integrated circuits, our results will also pave the way for on-chip phonon spin manipulation.

Spin and orbital degrees of freedom are two fundamental properties in describing vector wave fields such as light (1). The interaction between these two, termed spin–orbit interaction (SOI) (2), is crucial in elucidating the characteristics of vector wave fields. In systems exhibiting SOI, the wave spin can significantly influence and even govern the propagation behavior in space (i.e., spin-controlled orbit), and vice versa. Therefore, SOI-related phenomena present numerous opportunities for precise wave manipulation. A well-known and significant example of this is SOI in optics (3). For instance, the spin-Hall effect of light (4–6), stemming from optical SOI, induces spin-momentum locking (7), facilitating the robust manipulation of surface modes (8–12). When incorporated with thin film systems, SOI of light also introduces pioneering techniques in precision metrology (13, 14). Notably, within waveguides (WG) systems, SOI of light engenders spin-controlled unidirectional excitation (15), chiral coupling with nano-particles (16), spin-dependent directional scattering (17), and vortex beam generation (18). These studies demonstrate that delving into SOI opens avenues for innovative wave manipulation techniques.

Elastic waves, similar to electromagnetic waves, are vector wave fields that carry both spin and orbital degrees of freedom, enabling them to transport both spin angular momentum (SAM) and orbital angular momentum (OAM) (19–22). Elastic waves can be considered as acoustic phonons (22). In on-chip phononic circuits (23, 24), elastic WG act as essential components, wherein the spin and orbit degrees of freedom allow for direct manipulation of phonons. Notably, elastic spin offers more flexibility than spin in electromagnetic wave. For instance, in one-dimensional WG, where electromagnetic waves form a divergence-free field, the wave spin typically aligns parallel to the wave direction, known as longitudinal spin. On the other hand, the elastic displacement field consists of two components (19, 25, 26): a divergence-free component similar to electromagnetic waves and a curl-free component resembling acoustic waves. Thus, even within a one-dimensional elastic WG, elastic spin includes both longitudinal and transverse components. Therefore, SOI in elastic WG can introduce spin-related phenomena distinct from other WG systems, providing methods for exploring wave manipulation techniques.

Mounting the system on a rotating stage is a straightforward approach for observing phononic SOI in elastic WG (23). In this scenario, a frequency shift comparable to the working frequency (MHz) of the phononic WG requires an ultrafast rotation, posing significant challenges on the present sub-Hz rotating platform. This prompts

Author contributions: C.Y. and J.R. designed research; C.Y. performed research; C.Y. and J.R. analyzed data; and C.Y. and J.R. wrote the paper.

The authors declare no competing interest.

This article is a PNAS Direct Submission. G.M. is a guest editor invited by the Editorial Board.

[1]To whom correspondence may be addressed. Email: xonics@tongji.edu.cn.

This article contains supporting information online at https://www.pnas.org/lookup/suppl/doi:10.1073/pnas.2411427121/-/DCSupplemental.

Published November 15, 2024.

an intriguing question: Is there any intrinsic elastic SOI by leveraging the rich structure of the elastic wave field, without resorting to temporal spinning of the system?

In this study, we demonstrate the elastic SOI in helical WG, as well as its impact on the angular momentum (AM) structures and transport properties of elastic waves. With the help of the Timoshenko beam theory (27–30), we demonstrate the nontrivial elastic SOI as the gauge potential arising from the helical rotation of the local frame along the WG. We illustrate that a helical elastic WG can selectively convey phonon spin carried by elastic wave according to the chirality of WG, i.e., Chirality-Induced Phonon Spin Selectivity (CIPSS). These results advance the understanding of SOI in elastic waves, offering an approach for manipulating AM and transport in elastic systems.

The rest of the paper is organized as follows: 1) We begin by introducing the fundamental concept of AM and establishing the correlation between the displacement field and the AM. 2) Next, we showcase the SOI and the AM induced by SOI in a helical WG. 3) Finally, we demonstrate the CIPSS-induced phenomena, which encompasses the chirality-dependent output spin and spin-dependent transmission.

Elastic Field and AM in Curved Timoshenko Beam

The elastic WG can be defined by a parametric curve along the central of cross-sections (CS). For each CS, a local orthogonal coordinate system 123 is established (Fig. 1*A*), where the origin of coordinates is the geometric center of CS and 3-axis is perpendicular to the CS, denoted as η. We will focus on circular CS with a radius of r_0. The CS are indeformable in the Timoshenko beam model. Therefore, the state of a CS can be described by two vectors: translation $\boldsymbol{u} = u_j \boldsymbol{e}_j$ and rotation $\boldsymbol{\theta} = \theta_j \boldsymbol{e}_j$, $j = 1, 2, 3$. As such, the elastic waves propagating along WG can be expressed as $|\psi\rangle = |u\rangle \oplus |\theta\rangle = \sqrt{\rho\omega/2}\{u_1, u_2, u_3, \theta_1, \theta_2, \theta_3\}^T \exp(ik_\eta \eta - i\omega t)$, which contains both the translation $|u\rangle = \sqrt{\rho\omega/2}\{u_1, u_2, u_3\}^T \exp(ik_\eta \eta - i\omega t)$ and rotation $|\theta\rangle = \sqrt{\rho\omega/2}\{\theta_1, \theta_2, \theta_3\}^T \exp(ik_\eta \eta - i\omega t)$ information. Here, k_η is the wavenumber, η is the arc length along 3-axis, ω is the angular frequency, ρ is the mass density, and t is time. In the following text, we will omit $\sqrt{\rho\omega/2}$ and $\exp(ik_\eta \eta - i\omega t)$ for brevity.

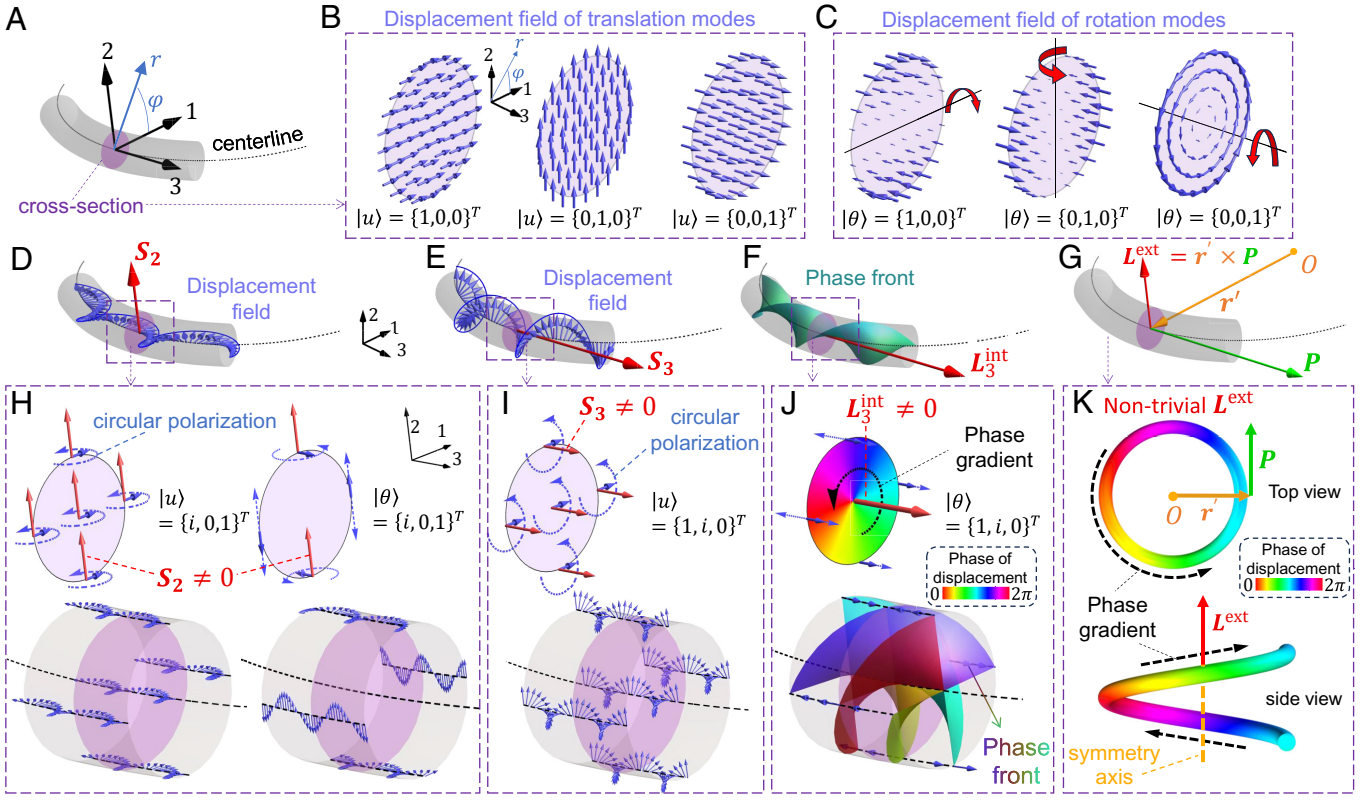

Fig. 1. Illustration of AM in rod-like elastic WG. (*A*) The elastic WG can be defined by a parametric curve along the central of CS (centerline). The local coordinate system 123 is shown by black arrows. Polar coordinate r and φ are defined in 1 to 2 plane. (*B* and *C*) Displacement fields over CS, where $|u\rangle \neq 0$, $|\theta\rangle = 0$ and $|u\rangle = 0$, $|\theta\rangle \neq 0$ are translation and rotation modes, respectively. $|u\rangle = \{1, 0, 0\}^T$ and $|u\rangle = \{0, 1, 0\}^T$ are shear modes, $|u\rangle = \{0, 0, 1\}^T$ is extensional mode, $|\theta\rangle = \{1, 0, 0\}^T$ and $|\theta\rangle = \{0, 1, 0\}^T$ are flexural modes, and $|\theta\rangle = \{0, 0, 1\}^T$ is torsion mode. Blue arrows show the displacement field. (*D*) The transverse elastic spin $\boldsymbol{S}_2$ (red solid arrow) arises from the circular polarization of the displacement field (solid blue arrows) in 1 to 3 plane. (*E*) The longitudinal elastic spin $\boldsymbol{S}_3$ arises from the circular polarization of the displacement field in 1 to 2 plane. (*F*) The Spiral phase front inside WG results nonzero intrinsic OAM $\boldsymbol{L}_3^{\text{int}}$ along 3-axis. (*G*) Demonstration of extrinsic OAM $\boldsymbol{L}^{\text{ext}}$. Here, P is the momentum of wave, $\boldsymbol{r}'$ is the distance vector point from O to field point. (*H*) Polarization of displacement field and elastic spin of states $|u\rangle = \{i, 0, 1\}^T$ and $|\theta\rangle = \{i, 0, 1\}^T$. The displacement field (solid blue arrows) is displayed on five position: the central, *Top*, *Bottom*, *Left*, and *Right* of WG. The linear or circularly polarization is highlight by the straight or circularly dashed blue arrows, respectively. Red solid arrows show the transverse elastic spin $\boldsymbol{S}_2$. (*I*) Polarization of displacement field and elastic spin of states $|u\rangle = \{1, i, 0\}^T$. This state results in an anticlockwise polarization in 1 to 2 plane, and possesses nonzero longitudinal elastic spin $\boldsymbol{S}_3$. (*J*) State $|\theta\rangle = \{0, 1, i\}^T$ leads to the circular phase gradient and the spiral phase front inside WG, associating with nonzero IOAM $\boldsymbol{L}_3^{\text{int}}$ along 3-axis. (*K*) Spiral trace of elastic wave in helical WG results in circular phase gradient (*Top* view), associating with nontrivial EOAM along the helical symmetry axis.

Fig. 1 *B* and *C* shows the displacement field for six typical states: three pure translation states with the homogeneous displacement field across the CS, and three pure rotation states where the displacement field is zero at the axis of rotation. The circular polarization of displacement fields results in nonzero elastic spin (19), which can either perpendicular to the wave direction ($\boldsymbol{S}_1$ and $\boldsymbol{S}_2$, Fig. 1*D* demonstrate $\boldsymbol{S}_2$ as an example) or parallel to the wave direction ($\boldsymbol{S}_1$, as shown in Fig. 1*E*). In Timoshenko beam, both rotation and translation states can results in circularly polarized displacement field and nonzero spin, as shown in Fig. 1 *H* and *I*.

The SAM of $|\theta\rangle = \{1, i, 0\}^T$ is zero. This is because the displacements are all linear polarized in this state. In fact, $|\theta\rangle = \{1, i, 0\}^T$ contains nonzero OAM. The difference between SAM and OAM lies in the types of rotation of displacement field (22): SAM pertains to the local rotation of displacement vectors, whereas OAM relates to the global rotation of the displacement field around a given reference point. As depicted in Fig. 1*C*, after an anticlockwise rotation of 90 degrees, $|\theta\rangle = \{1, 0, 0\}^T$ is same with $|\theta\rangle = \{0, 1, 0\}^T$. Consequently, $|\theta\rangle = \{1, i, 0\}^T$ represents $|\theta\rangle = \{1, 0, 0\}^T$ rotating anticlockwise around the center of the CS. This global rotational evolution gives rise to spiral phase front inside WG and results in a nonzero intrinsic OAM (IOAM), as shown in Fig. 1*J*.

Besides IOAM, there also exists another OAM from the perspective in global coordinate system (Fig. 1*G*). Considering a helical WG as an example (Fig. 1*K*), where elastic wave is restricted into a spiral profile. The helical propagation route also results in the rotational evolution, with the center of rotation situated at the helical symmetry axis. Unlike IOAM, where the rotation center is within the CS, the helical symmetry axis lies outside the CS. Thus, this type of OAM is termed extrinsic OAM (EOAM). The detailed calculation of displacement field $\boldsymbol{u}'(r, \varphi)$, total SAM ($\tilde{\boldsymbol{S}}$), IOAM ($\tilde{L}_3^{\text{int}}$), and EOAM ($\tilde{L}^{\text{ext}}$) over the CS can be found in *Materials and Methods* (Calculation of AM).

Spin–Orbit Interactions and AM Structure in Helical WG

Given a helical WG with infinite length and a radius r_0 of CS (Fig. 2*A*). To capture the dynamic state along a continuously differentiable curve, a natural choice is to establish the Frenet–Serret frame, which comprises tangent ($\boldsymbol{e}_3 = \partial\boldsymbol{\Xi}/(\partial\eta)$), normal ($\boldsymbol{e}_1 = \partial\boldsymbol{e}_3/(\kappa\partial\eta)$), and binormal ($\boldsymbol{e}_2 = \boldsymbol{e}_3 \times \boldsymbol{e}_1$) unit vectors of local coordinate system. The local basis obey the frame rate equation as : $\partial_\eta \boldsymbol{e}_1 = \tau\boldsymbol{e}_2 - \kappa\boldsymbol{e}_3$, $\partial_\eta \boldsymbol{e}_2 = -\tau\boldsymbol{e}_1$ and $\partial_\eta \boldsymbol{e}_3 = \kappa\boldsymbol{e}_1$, where τ and κ are the torsion $\tau = \sigma\sin(\Theta)\cos(\Theta)/R$ and curvature $\kappa = \sigma\cos^2(\Theta)/R$ of centerline, respectively. Here, $\sigma = 1$ or -1 represents the right or left-handed helix, respectively. According to the frame rate equation, the differential of a vector state of CS $\boldsymbol{v}$ (Here, $\boldsymbol{v}$ can denote both $\boldsymbol{u}$ and $\boldsymbol{\theta}$) with respect to η can be decomposed into two parts: derivation of individual components $\boldsymbol{e}_j\partial_\eta v_j$ and overall rotations $v_j\partial_\eta \boldsymbol{e}_j$. Therefore, $\partial_\eta \boldsymbol{v}$ can be represented as $i\hat{p}_\eta\,|v\rangle - i(\kappa\hat{S}_2 + \tau\hat{S}_3)\,|v\rangle$, where $\hat{p}_\eta = -i\partial_\eta$ is the momentum operator and $\hat{S}_j (j = 1, 2, 3)$ are spin-1 operators. After some algebra based on the kinematics of spatial rods (27, 29), synthetic gauge potential terms such as $\hat{S}_j\hat{p}_\eta$ will arise in the dynamic equation (*Dynamic Equations of Timoshenko Theory in Helical WG*), finally expressed as

$$\boldsymbol{C}\omega^2|\psi\rangle = \left(\mathcal{H}_0 + \boldsymbol{A}\otimes\hat{\boldsymbol{S}}_2\hat{p}_\eta + \boldsymbol{B}\otimes\hat{\boldsymbol{S}}_3\hat{p}_\eta + \mathcal{K}\right)|\psi\rangle, \quad [1]$$

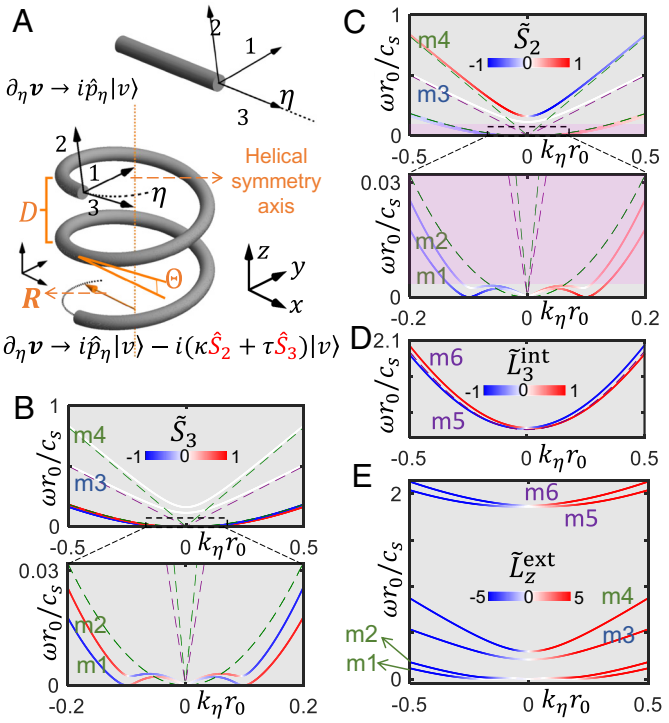

Fig. 2. SOI in helical WG. (*A*) Illustration of straight and *Right*-handed helical WG. The origin of local coordinate system is located on the centerline. In helical WG, axis 1, 2, and 3 are normal, binormal, and tangent axis of Frenet–Serret basis, respectively. In helical WG, the rotation of local coordinate system results in extra term in $\partial_\eta \boldsymbol{v}$, which eventually leads to the synthetic gauge potential in dynamic equation. (*B–E*) The dispersion relations of a straight WG (dashed lines) and *Right*-handed helical WG (solid lines), where c_s denotes the speed of shear waves. AM in helical WG is depicted using red-blue colors. Modes of helical WG are labeled as m1 to m6. Results are calculated based on properties of copper and $R = D = 10r_0 = 0.001$m. All data of AM in figures have been divided by $|\tilde{\boldsymbol{u}}'|^2$, where $|\tilde{\boldsymbol{u}}'|^2 = \int_0^{r_0}\int_0^{2\pi}|\boldsymbol{u}'|^2 r d\varphi dr$ relates to the total intensity of vibration. $\tilde{S}_1$ is always zero and is not depicted here. (*B* and *C*) Dispersion distribution of $\tilde{S}_3$ and $\tilde{S}_2$, respectively. Modes m5 and m6 possess zero spin and are not depicted here. (*D*) IOAM $\tilde{L}_3^{\text{int}}$ of m5 and m6. Modes m1 to m4 possess zero IOAM and are not depicted here. (*E*) EOAM $\tilde{L}_z^{\text{ext}}$ of all modes. EOAM mainly depending on k_η and the chirality of the WG, and the $\tilde{L}_z^{\text{ext}}$ of all modes are similar.

where $\otimes$ means the Kronecker product, $\boldsymbol{C}$ contains the mass and moment of inertia of CS, $\mathcal{H}_0$ is the dynamic matrix of the corresponding straight rod, $\mathcal{K}$ contains constant potential terms associated with the torsion and curvature of the helix rod, which is independent of k_η. The emerged second and third terms on the right side of Eq. **1** are the helix-induced gauge potentials that introduce elastic SOI, wherein

$$\boldsymbol{A} = -\kappa\begin{pmatrix}\alpha_p + \alpha_s & 0\\ 0 & \beta_t + \beta_f\end{pmatrix}; \boldsymbol{B} = -\tau\begin{pmatrix}2\alpha_s & 0\\ 0 & 2\beta_f\end{pmatrix}.$$

α_s, α_p, β_f, and β_t represent the shear, extensional, flexural, and torsional rigidity, respectively. Clearly, reversing the helicity σ will reverse the sign of κ and τ, as well as the sign of elastic SOI terms.

Eq. **1** results in six eigenmodes. In a straight WG, modes m1 and m2 are transversely polarized and always degenerate. In the helical WG, the $\hat{\boldsymbol{S}}_3\hat{p}_\eta$ term separates m1 and m2, creating a nonzero longitudinal SAM, leading to different phase velocities for clockwise and anticlockwise circular polarizations. This causes the phase difference to vary with transmission distances. Research has shown that in a helical WG, the geometric phase can alter the

polarization angle of linear oscillation (31). Linear polarization is a mix of clockwise and anticlockwise circular polarizations, where the linear polarization angle is tied to the phase difference between these two polarizations. Therefore, the splitting of m1 and m2 indicates changes in the linear polarization angle, associating with the geometric phase in helical WG. In the low-frequency range, the spectra of modes m1 and m2 exhibit a local maximum followed by a local minimum as k_η increases, reminiscent of the "roton-like" behavior demonstrated in metamaterials (32) and micropolar crystal (33). Related mode shape of m1 and m2 at low frequency can be found in *SI Appendix*.

The SOI in elastic WG not only influence the longitudinal spin but also separate the transverse spin states of extension mode (m4) and shear modes (m1 and m2) near $k_\eta = 0$. In a straight WG, the extensional mode (m4) and the shear modes (m1, m2) are degenerate at $k_\eta = 0$. Consequently, near $k_\eta = 0$ in helical WG, $\hat{\boldsymbol{S}}_2\hat{p}_\eta$ term can mix the extensional and shear modes, giving rise to nonzero transverse SAM $\tilde{S}_2$, as illustrated in Fig. 2*C*. Below the cut-off frequency of m3, only m1 and m2 exist, displaying a spin-momentum locking feature: Within the frequency range highlighted by a purple background in Fig. 2*C*, the sign of $\tilde{S}_2$ is locked with the sign of group velocity. This implies a spin-dependent unidirectional excitation in elastic helical WG (*SI Appendix*, Fig. S4).

Besides SAM, the elastic SOI $\hat{S}_3\hat{p}_\eta$ in Eq. **1** will also result in nonzero IOAM. The originally degenerate modes m5 and m6 are separated by the helical-induced SOI into two modes with opposite IOAM, as shown in Fig. 2*D*. This mode's splitting is due to the geometric phase resulting from the synthetic gauge potential, akin to the splitting of modes with opposite $\hat{S}_3$. Research has been conducted on the splitting of OAM-related modes in helical acoustic WG (34), known as the "acoustic spin-redirection phase." Similar phenomena also discussed in optics as "orbit–orbit interaction" (3, 35, 36). The geometric phase phenomenon related to IOAM in helical elastic WG is analogous to those observed in air acoustics and optics (*SI Appendix*, Fig. S5).

The EOAM along z-axis $\tilde{L}_z^{\text{ext}}$ of right-handed WG is shown in Fig. 2*E*. $\tilde{L}_z^{\text{ext}}$ of all modes are dependent on k_η. The magnitude of EOAM will increase along with k_η, and the sign of EOAM is locked with the sign of k_η. In conjunction with SAM and IOAM, we can calculate the total AM carried by elastic waves in a helical WG, with its component in the z-direction denoted as $\tilde{J}_z = \tilde{S}_2\cos(\Theta) + (\tilde{S}_3 + \tilde{L}_3^{\text{int}})\sin(\Theta) + \tilde{L}_z^{\text{ext}}$. As such, by taking account the conservation of total AM, one could analyze the AM related phenomena in composite WG.

Chirality-Induced Phonon Spin Selectivity in Composite Elastic WG

Consider a straight WG extending along the z-direction. In this WG, the z-directional EOAM is zero due to the straight propagation path of elastic waves. Additionally, within the low-frequency range (modes m1-m4), the IOAM is zero. As such, the total AM along the z-direction equals to $\tilde{S}_z$. Waves with anticlockwise polarization in x-y plane have positive $\tilde{S}_z$, while waves with clockwise polarization have negative $\tilde{S}_z$.

For a helical WG, in the absence of m5 and m6, the total AM encompasses SAM and EOAM. In pure helical WG, the group velocity locked with $\tilde{J}_z$ (*SI Appendix*, section 5). Consequently, a right-handed helical WG can only propagate waves with positive AM in the forward direction. Conversely, a left-handed helical WG can only propagate waves with negative AM. Therefore, embedding a section of a helical WG within a straight WG yields the CIPSS phenomena: 1) creating linearly polarized oscillation in the straight WG segment results in an input signal with zero $\tilde{S}_z$; 2) Since the right-handed helical WG can only transmit waves with positive AM, elastic waves output from the helical section to the straight WG will also possess a positive AM; 3) As such, the transmitted signal in straight WG will possess positive $\tilde{S}_z$, implies anticlockwise polarization in x-y plane. Here, we illustrate an example of a composite WG with a gradually changing R, as depicted in Fig. 3*A*.

Fig. 3 *B* and *C* provides an example of CIPSS about chirality-dependent output spin at $\omega r_0/c_s = 0.3$. The excitation point is situated at $z = -10D$, employing a pulse-like signal proportional to $\sin(2\pi f_0 t)gp(t)$. Here, t denotes time, f_0 is the central frequency of the input, related to the angular frequency as $\omega = 2\pi f_0$, and $gp(t)$ represents the Gaussian pulse located at $4/f_0$ with a SD of $1/f_0$. The utilization of this pulse-like signal helps avoid the effects of boundary reflections, aiding in distinguishing between the original signal and reflections.

The output is measured at $Z = 5D$. The time-domain displacement plot in Fig. 3*C* illustrates that u_y has a phase delay relative to u_x in right-handed WG and a phase lead relative to u_x in left-handed WG. The polarization profile for a single period is shown besides the time-domain plots. It shows anticlockwise polarization for right-handed WG and clockwise polarization for left-handed WG. Thus, the output $\tilde{S}_z$ is positive and negative in right-handed and left-handed composite WG, respectively.

Fig.3*D* illustrates the relationship between the output spin and the frequency. We perform a Fourier transform on the time-domain signal obtained at $z = 5D$ to extract the complex amplitudes of displacement along the x and y directions. From this, we calculate the value of the normalized $\tilde{S}_z$. When $\tilde{S}_z$ approaches 0, it indicates that the signal tends toward linear polarization, i.e., the weaker the CIPSS effect; as $\tilde{S}_z$ approaches 1, it suggests that the output signal tends toward circular polarization, indicating a stronger CIPSS effect. The CIPSS effect becomes more pronounced as the frequencies increase. This is because $\tilde{J}_z$ in the helical WG increases with frequency (*SI Appendix*, section 5).

In addition to the chirality-dependent spin of output, CIPSS can also determine the transmission rate based on the spin of the input. Illustrated in Fig. 4, we demonstrate this effect using a right-handed composite WG as an example. Excitation of nonzero spin signals can be achieved by simultaneously applying excitation in the x and y directions, as shown in Fig 4*A*. Fig. 4 *B* and *C* show the snapshots of simulations. In the right-handed WG, the positive group velocity relates to positive AM. Thus, input signals with negative $\tilde{S}_z$ cannot smoothly pass through the right-handed section in composite WG. Therefore, the output magnitude of signal with positive $\tilde{S}_z$ is higher than that of signal with negative $\tilde{S}_z$. Fig. 4*D* shows the output recording at $z = 5D$. The polarization direction of outputs is same with the inputs, as well as the sign of $\tilde{S}_z$. Meanwhile, magnitude of output with $\tilde{S}_z < 0$ is lower than that of output with $\tilde{S}_z > 0$, which shows the spin-dependent transportation.

The transmission rate with different frequency is shown in Fig. 4*E*. As the frequency approaches zero, transmission rate of both positive and negative $\tilde{S}_z$ are approaching 1, and the CIPSS effect is not significant at low frequencies. With increasing frequency, the transmission rate of negative $\tilde{S}_z$ decreases, while signals with positive $\tilde{S}_z$ maintain a higher transmission rate. This indicates that the CIPSS effect strengthens with increasing

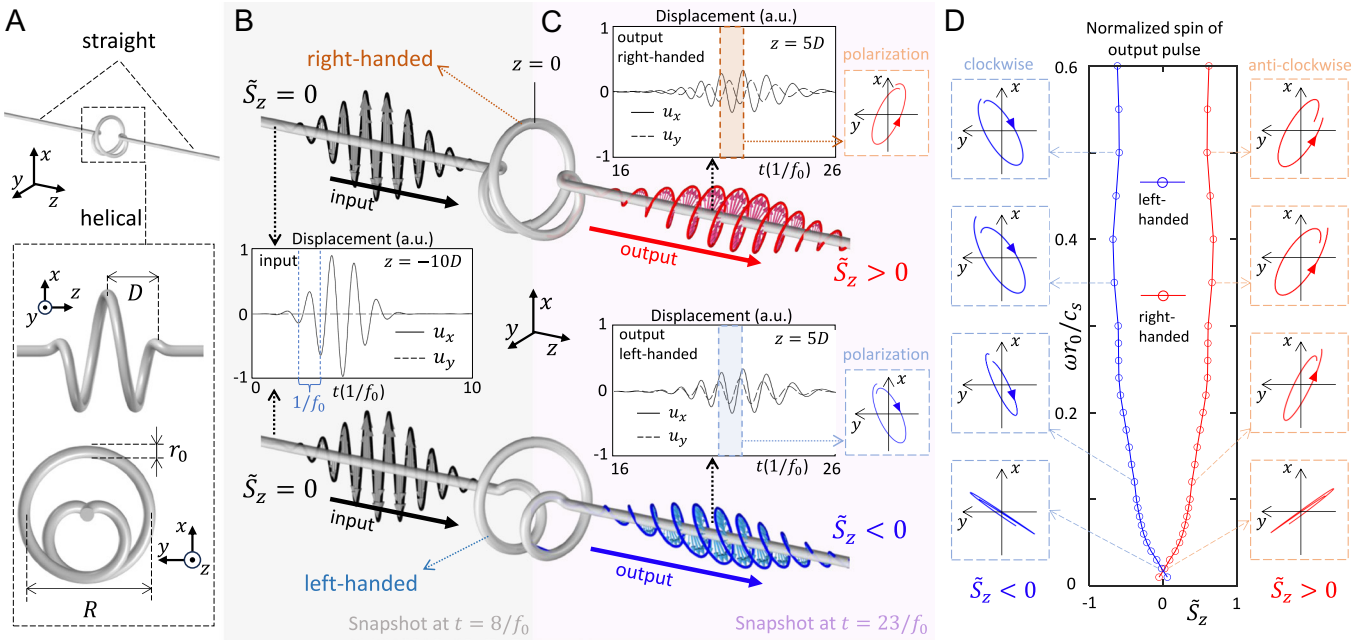

Fig. 3. Demonstration of CIPSS about chirality-dependent output spin. (*A*) Illustration of straight–helical–straight WG. The simulation parameters include: $R = D = 10\ r_0 = 0.001$ m; material properties are $\rho = 8{,}960$ kg/m^3, $E = 110$ GPa and $\nu = 0.35$, corresponding to the parameters of copper. See *SI Appendix*, section 5 for the parametric equations about position of centerline. (*B*) Demonstration of CIPSS through a composite WG at $\omega r_0/c_S = 0.3$. Simulation results are presented as snapshots and time-domain displacement plots. The black, red, and blue curves in snapshots illustrate the displacement profiles of the signals. The linear excitation is applied at $z = -10D$. A pulse-like input is selected to avoid the impact of boundary reflections, facilitating the difference between the original signal and reflections. The center frequency of excitation is $f_0 = 2\pi\omega$. (*C*) Snapshots and time-domain displacement plots of outputs. The time-domain signal is recorded at $z = 5D$. Displacement plots indicate the nonzero Spin. For example, in the output signal of *Right*-handed composite WG, the phase of u_y is delayed by approximately $\pi/2$ compared to u_x, indicating the anticlockwise polarization and positive $\tilde{S}_z$. (*D*) Normalized $\tilde{S}_z$ at $z = 5D$ for *Right* and *Left*-handed composite WG. Insertions shows the polarization at $\omega r_0/c_S = 0.02$, 0.12, 0.35, and 0.5, respectively. As the frequency increases, the output signal transitions from linear polarization to circular polarization, signifying that the efficiency of CIPSS increases with higher frequencies.

frequency, consistent with the results in Fig. 3*D*. However, as the frequency continues to rise, the transmission rate of $\tilde{S}_z$ signals shows an upward trend again. This is due to the involvement of the torsional mode. As the input signal frequency gradually increase, the circularly polarized input will apply torque along z-axis on helical section, which induce the torsional waves on output side. Therefore, the transmission rate of signals with negative $\tilde{S}_z$ shows a trend of initially decreasing and then increasing as frequency increases (See *SI Appendix*, section 5 for magnitude of torsion mode on output side). This will not affect the chirality-dependent spin of output in Fig. 3 because the pure torsion mode carries zero spin.

Discussions

By applying the Timoshenko model, we have analytically obtained elastic SAM and OAM according to the dynamic equation of helical WG. Within the frequency range presented in the main text, the Finite Element Method results show good agreement with the analytical theory (*SI Appendix*, section 6). However, the Timoshenko model assumes a nondeformable CS, thus limiting its scope to consider higher-order states. Through simulation, we can obtain information on vibration modes at higher frequencies (*SI Appendix*, section 7). It has been demonstrated that at higher frequencies, the presence of inhomogeneous properties in a straight rod leads to unidirectional routing, as shown in ref. 37. In future studies, one can explore the SOI of high-frequency modes in helical rods, which also exhibit richer angular momentum structures.

It is evident from our work, acoustics system (34) and optics system (3) that equivalent rotation resulting from the chirality is closely associated with SOI of waves. Hence, it is natural to anticipate that SOI in elastic waves are widespread in chiral systems. For example, in the examination of elastic metamaterials, chiral metamaterials have the capability to display circular dichroism (38, 39), indicating that chiral metamaterials can also serve as arenas for investigating SOI in elastic waves.

In addition to the nonzero spin in the rod-like WG studied in this work, surface guided modes like Rayleigh-Lamb modes also show spin-momentum locking and spin-controlled unidirectional excitation (40–42). The difference between Rayleigh-Lamb modes and SOI in a helical waveguide lies in: 1) Rayleigh-Lamb modes, the spin is perpendicular to the wave direction. In contrast, in a helical waveguide, the spin can point in any direction. 2) The SOI in a helical waveguide are introduced by the synthetic gauge potential. This potential splits degenerate modes, resulting in nonzero spin. In Rayleigh-Lamb modes, the spin is not related to the "mode splitting." Another contrast exists between elastic spin in continuous solids and pseudospin in topological WG. Topological WG exhibit pseudo-spin-dependent chiral modes and topological protection (43–45). However, when considering elastic spin, the eigen modes within topological WG often display multiple spin directions (46, 47), making it challenging to efficiently transport "pure" elastic spin through topological WG.

In future research, existing experimental techniques can be referenced to experimentally verify phenomena such as unidirectional excitation and CIPSS. A spin source required for achieving unidirectional excitation can be implemented using a chiral source composed of a pair of piezoelectric patches (37). Measurements of elastic wave spins can be conducted using a laser vibrometer (25) or a pair of accelerometers (31). Additionally,

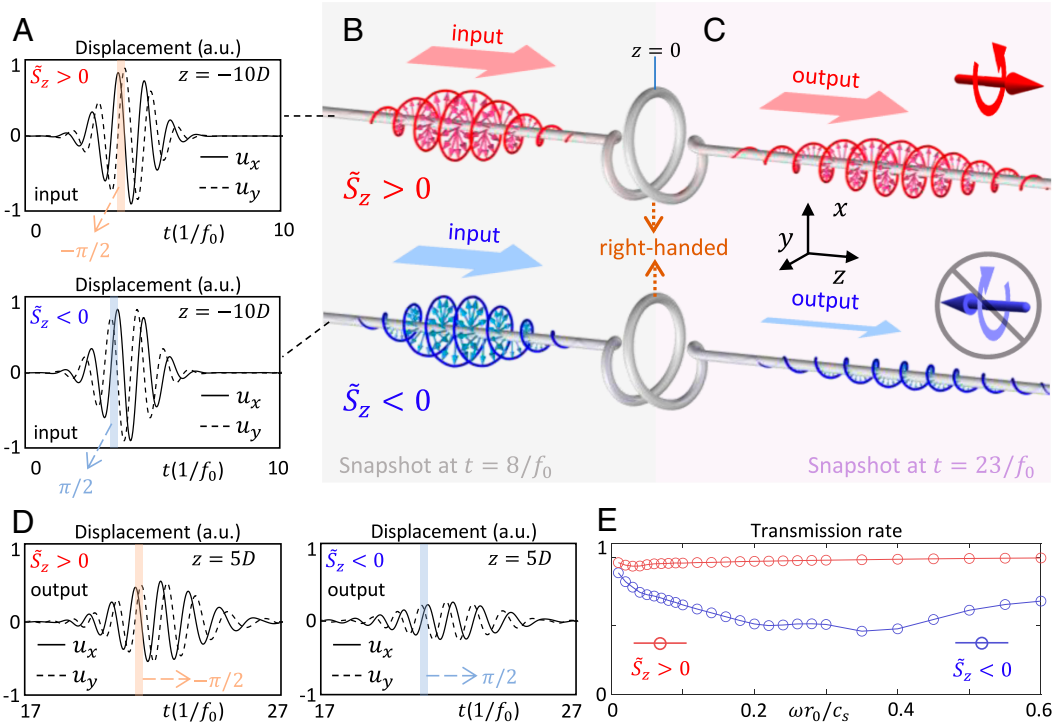

Fig. 4. Demonstration of CIPSS about spin-dependent transportation. (*A–D*) Demonstration of CIPSS with nonzero-spin-input at $\omega r_0/c_s = 0.3$ for *Right*-handed composite WG. Simulation results are presented as snapshots and time-domain displacement plots. (*A*) *Upper* and *Lower* panels show the displacement of input at excitation point $z = -10D$ with positive and negative $\tilde{S}_z$, respectively. The circularly polarized input can realized by a pair of force along x and y axes. Here, the phase of u_y differ from u_x with $-\pi/2$ and $\pi/2$, associating with positive and negative $\tilde{S}_z$, respectively. (*B*) Snapshots of inputs at $t = 8/f_0$. The red and blue curves in snapshots illustrate the displacement profiles with positive and negative $\tilde{S}_z$, respectively. (*C*) Snapshots of outputs at $t = 23/f_0$. The magnitude of output with negative $\tilde{S}_z$ is weaker than that of positive $\tilde{S}_z$, which highlight the CIPSS effect. (*D*) The time-domain signal recording at $z = 5D$. The spin of output signals are same with input ones. (*E*) transmission rate of signal with positive and negative spin. The transmission rate is defined as $|\tilde{\boldsymbol{u}}'_{tr}|^2/(|\tilde{\boldsymbol{u}}'_{tr}|^2 + |\tilde{\boldsymbol{u}}'_{re}|^2)$, where $|\tilde{\boldsymbol{u}}'_{tr}|^2$ and $|\tilde{\boldsymbol{u}}'_{re}|^2$ represent the magnitudes of the displacement field of the transmitted and reflected pulse, respectively.

for on-chip devices, excitation and measurement can be achieved with optomechanics (48, 49) or magnetoelasticity (50–52).

In conclusion, our study has illustrated the presence of elastic SOI in helical WG. We have demonstrated that the synthetic gauge potential within helical WG introduces elastic SOI and nontrivial elastic AM profiles, significantly influencing the propagation of elastic waves. Through both theoretical analysis and simulations, we have elucidated the interplay between elastic SAM, IOAM, and EOAM induced by elastic SOI. Results show that the AM structure within helical elastic WG can induce the CIPSS, enhancing our comprehension of SOI in elastic WG and presenting strategies for manipulating elastic waves based on angular momentum.

Materials and Methods

Calculation of AM. Calculating AM needs the displacement field of the CS. The displacement field at the center point of a CS equals the translation $\boldsymbol{u}$. However, the displacements of other points on the CS are not only influenced by translation but also by rotation. We use $\boldsymbol{u}'(r,\varphi) = u'_1(r,\varphi)\boldsymbol{e}_1 + u'_2(r,\varphi)\boldsymbol{e}_2 + u'_3(r,\varphi)\boldsymbol{e}_3$ to denote the displacement at point (r,φ). Here, (r,φ) are the polar coordinates in 1 to 2 plane. For small vibrations, the displacement vector field over CS is $\boldsymbol{u}'(r,\varphi) = u'_1\boldsymbol{e}_1 + u'_2\boldsymbol{e}_2 + u'_3\boldsymbol{e}_3$, which relates to translation and rotation as

$$\begin{aligned} u'_1 &= u_1 - \theta_3 r\sin(\varphi), \\ u'_2 &= u_2 + \theta_3 r\cos(\varphi), \\ u'_3 &= u_3 + \theta_1 r\sin(\varphi) - \theta_2 r\cos(\varphi), \end{aligned} \quad [2]$$

where r and φ are polar coordinates in the plane perpendicular to 3-axis.

Given a 3-dimension state $|v\rangle = \{v_1, v_2, v_3\}^T$, $\langle v|\hat{S}_j|v\rangle$ results in circular polarization strength of $|v\rangle$ in j direction. For instance, state vector $|v\rangle = \{1, \pm i, 0\}^T$, which means v_2 has $\pm\pi/2$ phase different from v_1, leads to $\langle v|\hat{S}_3|v\rangle = \pm 1$. The physical meaning of this "circular polarization" depends on the meaning of $\boldsymbol{v}$. Spin-1 operators are :

$$\hat{S}_1 = -i\begin{pmatrix} 0 & 0 & 0 \\ 0 & 0 & 1 \\ 0 & -1 & 0 \end{pmatrix}; \hat{S}_2 = -i\begin{pmatrix} 0 & 0 & -1 \\ 0 & 0 & 0 \\ 1 & 0 & 0 \end{pmatrix},$$
$$\hat{S}_3 = -i\begin{pmatrix} 0 & 1 & 0 \\ -1 & 0 & 0 \\ 0 & 0 & 0 \end{pmatrix}. \quad [3]$$

Based on $\boldsymbol{u}'$, we can derive the elastic SAM density $\boldsymbol{S} = \frac{\rho\omega}{2}\mathrm{Im}[\boldsymbol{u}'^* \times \boldsymbol{u}']$ (19, 21, 22), where * denotes the complex conjugate and $\mathrm{Im}[\cdot]$ is imaginary part. The total SAM carried by a CS can be integrated as $\tilde{S}_j = \int_0^{r_0}\int_0^{2\pi} S_j r d\varphi dr$, so that:

$$\begin{aligned} \tilde{S}_1 &= \pi r_0^2\langle u|\hat{S}_1|u\rangle + \frac{\pi r_0^4}{4}\langle\theta|\hat{S}_1|\theta\rangle, \\ \tilde{S}_2 &= \pi r_0^2\langle u|\hat{S}_2|u\rangle + \frac{\pi r_0^4}{4}\langle\theta|\hat{S}_2|\theta\rangle, \\ \tilde{S}_3 &= \pi r_0^2\langle u|\hat{S}_3|u\rangle. \end{aligned} \quad [4]$$

Here, $\langle u|\hat{S}_j|u\rangle$ and $\langle\theta|\hat{S}_j|\theta\rangle$ results in circular polarization intensity of state $|u\rangle$ and $|\theta\rangle$ in j direction, respectively. Noting that in Eq. **4**, $\langle\theta|\hat{S}_3|\theta\rangle$ does not contribute to the SAM. This is because total SAM of states like $|\theta\rangle = \{1, i, 0\}^T$ are zero.

Elastic OAM density is given as (19–22): $\boldsymbol{L} = \boldsymbol{r} \times \boldsymbol{P}$, where $\boldsymbol{r}$ is the relative position vector from the reference point to the field point, $\boldsymbol{P} = \frac{\rho\omega}{2}\mathrm{Im}[\boldsymbol{u}'^* \cdot (\nabla)\boldsymbol{u}']$ is the linear momentum of elastic wave. For IOAM, the reference point is chosen as the center of CS. If $u'_1 = 0$, $u'_2 = 0$, and $u'_3 \neq 0$, the IOAM density can be represented as $L_3^{\mathrm{int}} = \frac{\rho\omega}{2}|u'_3|^2\partial_\varphi\phi$ (22), where ϕ is the phase of u'_3 with gradient along polar angle φ. From this form, one can clearly see the relation between phase and IOAM. Specifically, if we replace θ_1 and θ_2 with $\theta_+ = -\theta_2 - i\theta_1$ and $\theta_- = -\theta_2 + i\theta_1$, the displacement can be represented as $u'_3 = \frac{r}{2}(\theta_+ e^{i\varphi} + \theta_- e^{-i\varphi})$. As such, it is clear that θ_+ and θ_- refer to the amplitude of positive and negative IOAM. Accordingly, the IOAM density will be $L_3^{\mathrm{int}} = \frac{\rho\omega}{2}\frac{r^2}{4}(|\theta_+|^2 - |\theta_-|^2) = \frac{\rho\omega}{2}\frac{r^2}{2}\mathrm{Im}[\theta_1^*\theta_2 - \theta_2^*\theta_1] = \frac{r^2}{2}\langle\theta|\hat{S}_3|\theta\rangle$. Consequently, the IOAM of CS is given by

$$\tilde{L}_3^{\mathrm{int}} = \int_0^{r_0}\int_0^{2\pi} L_3^{\mathrm{int}} r d\varphi dr = \frac{\pi r_0^4}{4}\langle\theta|\hat{S}_3|\theta\rangle . \quad [5]$$

The formula for EOAM is dependent on geometric parameters, lacking a concise form. Therefore, only the calculation method will be provided here. The EOAM in respect to a reference axis is $\boldsymbol{L}^{\mathrm{ext}} = \boldsymbol{r}' \times \boldsymbol{P}$. Here, $\boldsymbol{r}'$ is the relative position vector from the reference point O to the field point. In the discussion of helical WG, we set O on the helical symmetry axis and, which is parallel to z-axis, and let $\boldsymbol{r}' \perp \boldsymbol{e}_z$. As such, $\tilde{\boldsymbol{L}}^{\mathrm{ext}} = \int_0^{r_0}\int_0^{2\pi}\boldsymbol{L}^{\mathrm{ext}} r d\varphi dr$ can be decomposed into $\tilde{L}_z^{\mathrm{ext}}\boldsymbol{e}_z$, which is parallel to the z-axis, and $\tilde{L}_\perp^{\mathrm{ext}}\boldsymbol{e}_\perp$ perpendicular to the z-axis. Given the helical symmetry of WG, integration of $\tilde{L}_\perp^{\mathrm{ext}}\boldsymbol{e}_\perp dz$ over a period of helix should equal zero, and only $\tilde{L}_z^{\mathrm{ext}}$ survives.

The IOAM of elastic wave is $\boldsymbol{L} = \boldsymbol{r} \times \boldsymbol{P}$, $\boldsymbol{r}$ is the distance vector point from center of CS to the field point, range from 0 to r_0. Similarly, EOAM is $\boldsymbol{L} = \boldsymbol{r}' \times \boldsymbol{P}$, but with a different distance vector $\boldsymbol{r}'$ range from $R - r_0$ to $R + r_0$. Thus, $\boldsymbol{r}'$ is much larger than $\boldsymbol{r}$. According to the definition $\boldsymbol{P} = \frac{\rho\omega}{2}\mathrm{Im}[\boldsymbol{u}'^* \cdot (\nabla)\boldsymbol{u}']$, the momentum component $P_3\boldsymbol{e}_3 = \frac{\rho\omega}{2}\sum_j(u'^*_j\partial_\eta u'_j)\boldsymbol{e}_3 \propto k_\eta$. Since $P_3\boldsymbol{e}_3$ aligns parallel to the 3-axis, it does not contribute to the IOAM $\tilde{L}_3^{\mathrm{int}}$, which is also along the 3-axis. In contrast, for the EOAM, $\boldsymbol{r}' \times P_3\boldsymbol{e}_3$ is nonzero and significantly influences the EOAM along z-axis. Therefore, at higher values of k_η, both the momentum and the distance vector associated with EOAM exceed those of IOAM, leading to a greater magnitude of EOAM compared to IOAM.

Dynamic Equations of Timoshenko Theory in Helical WG. The parametric equation for central line in the global coordinate system xyz is given as $\boldsymbol{\Xi}(\eta) = R\cos(2\sigma\pi\eta/\eta_0)\boldsymbol{e}_x + R\sin(2\sigma\pi\eta/\eta_0)\boldsymbol{e}_y + (D\eta/\eta_0)\boldsymbol{e}_z$. Here, $\sigma = 1$ or -1 represents the right or left-handed helix, respectively. R is the outer radius of the helix, D is the helical pitch and $\eta_0 = \sqrt{4\pi^2R^2 + D^2}$ is the arc length of each period. Let $\boldsymbol{u}$, $\boldsymbol{\theta}$, $\boldsymbol{Q}$ and $\boldsymbol{M}$ be vectors representing the translation, rotation, internal force, and internal moment, respectively. The strain vector and moment-strain vector are (30) $\boldsymbol{\varepsilon} = \partial_\eta\boldsymbol{u} + \boldsymbol{e}_3 \times \boldsymbol{\theta}$ and $\boldsymbol{\varepsilon}_\theta = \partial_\eta\boldsymbol{\theta}$, respectively. Strain and moment-strain can also be represented in operator form:

$$\begin{aligned}|\varepsilon\rangle &= i(\hat{p}_\eta - \kappa\hat{S}_2 - \tau\hat{S}_3)|u\rangle - i\hat{S}_3|\theta\rangle ,\\ |\varepsilon_\theta\rangle &= i(\hat{p}_\eta - \kappa\hat{S}_2 - \tau\hat{S}_3)|\theta\rangle .\end{aligned} \quad [6]$$

The relation between $|\varepsilon\rangle$, $|\varepsilon_\theta\rangle$ and internal force $|Q\rangle$, internal moment $|M\rangle$ are

$$|Q\rangle = \begin{pmatrix}\alpha_s & 0 & 0\\ 0 & \alpha_s & 0\\ 0 & 0 & \alpha_p\end{pmatrix}|\varepsilon\rangle ; |M\rangle = \begin{pmatrix}\beta_f & 0 & 0\\ 0 & \beta_f & 0\\ 0 & 0 & \beta_t\end{pmatrix}|\varepsilon_\theta\rangle , \quad [7]$$

where $\alpha_s = \frac{3E\pi r_0^2}{14(1+\nu)}$, $\alpha_s = E\pi r_0^2$, $\beta_f = \frac{E\pi r_0^4}{4}$ and $\beta_t = \frac{E\pi r_0^4}{4(1+\nu)}$. In this work, we set $r_0 = 1$ mm $\rho = 8{,}960\,\mathrm{kg/m^3}$, $E = 110$ GPa and $\nu = 0.35$, which are mass density, Young's modulus, and Poisson coefficient of copper, respectively. Accelerations of translation and rotation are related with $|Q\rangle$ and $|M\rangle$ as

$$\begin{aligned}-\omega^2 C_1|u\rangle &= i(\hat{p}_\eta - \kappa\hat{S}_2 - \tau\hat{S}_3)|Q\rangle ,\\ -\omega^2 C_2|\theta\rangle &= i(\hat{p}_\eta - \kappa\hat{S}_2 - \tau\hat{S}_3)|M\rangle - i\hat{S}_3|Q\rangle ,\end{aligned} \quad [8]$$

where C_1 and C_2 contains the mass and moment of inertia of CS as

$$C_1 = \rho\pi r_0^2\begin{pmatrix}1 & 0 & 0\\ 0 & 1 & 0\\ 0 & 0 & 1\end{pmatrix}; C_2 = \frac{\rho\pi r_0^4}{4}\begin{pmatrix}1 & 0 & 0\\ 0 & 1 & 0\\ 0 & 0 & 2\end{pmatrix}. \quad [9]$$

As such, by combining $|u\rangle$ and $|\theta\rangle$ into $|\psi\rangle$, Eqs. **6**–**9** results in

$$\boldsymbol{C}\omega^2|\psi\rangle = \left(\mathcal{H}_0 + \boldsymbol{A}\otimes\hat{\boldsymbol{S}}_2\hat{p}_\eta + \boldsymbol{B}\otimes\hat{\boldsymbol{S}}_3\hat{p}_\eta + \mathcal{K}\right)|\psi\rangle, \quad [10]$$

where:

$$\boldsymbol{C} = \begin{pmatrix}C_1 & 0\\ 0 & C_2\end{pmatrix},$$

$$\mathcal{H}_0 = \begin{pmatrix}\hat{p}_\eta^2\alpha_s & 0 & 0 & 0 & i\hat{p}_\eta\alpha_s & 0\\ 0 & \hat{p}_\eta^2\alpha_s & 0 & -i\hat{p}_\eta\alpha_s & 0 & 0\\ 0 & 0 & \hat{p}_\eta^2\alpha_p & 0 & 0 & 0\\ 0 & i\hat{p}_\eta\alpha_s & 0 & \beta_f\hat{p}_\eta^2 + \alpha_s & 0 & 0\\ -i\hat{p}_\eta\alpha_s & 0 & 0 & 0 & \beta_f\hat{p}_\eta^2 + \alpha_s & 0\\ 0 & 0 & 0 & 0 & 0 & \hat{p}_\eta^2\beta_t\end{pmatrix},$$

$$\mathcal{K} = \begin{pmatrix}\mathcal{K}_{11} & \mathcal{K}_{12}\\ \mathcal{K}_{21} & \mathcal{K}_{22}\end{pmatrix},$$

$$\mathcal{K}_{11} = \begin{pmatrix}\kappa^2\alpha_p + \tau^2\alpha_s & 0 & 0\\ 0 & \tau^2\alpha_s & -\kappa\tau\alpha_s\\ 0 & -\kappa\tau\alpha_s & \kappa^2\alpha_s\end{pmatrix},$$

$$\mathcal{K}_{21} = \begin{pmatrix}\kappa^2\beta_t + \tau^2\beta_f & 0 & 0\\ 0 & \tau^2\beta_f & -\kappa\tau\beta_f\\ 0 & -\kappa\tau\beta_f & \kappa^2\beta_f\end{pmatrix},$$

$$\mathcal{K}_{12} = (\mathcal{K}_{21})^T = \begin{pmatrix}\tau\alpha_s & 0 & 0\\ 0 & \tau\alpha_s & 0\\ 0 & -\kappa\alpha_s & 0\end{pmatrix}. \quad [11]$$

The dynamic equation Eq. **10** shows the relation between acceleration (left side) and the force (right side) with 6×1 vector $|\psi\rangle$ and 6×6 matrices. The off-diagonal element in matrix indicates the nonzero interactions between different degree of freedoms. For instance, in the matrix $\mathcal{H}_0$, the element $\mathcal{H}_0[1,5] = i\hat{p}_\eta\alpha_s$ implies that the force acting on the first degree of freedom (u_1) includes a component related to the fifth degree of freedom (θ_2) as $\mathcal{H}_0[1,5]\theta_2 = i\hat{p}_\eta\alpha_s\theta_2$, showing a nonzero interaction between u_1 and θ_2. These interactions between $|u\rangle$ and $|\theta\rangle$ results in the absence of modes with purely translation ($|\theta\rangle = 0$) or purely rotation ($|u\rangle = 0$). When the dispersion curves of the rotation and translation modes do not intersect, we can determine the mode category by examining the ratio of contributions from translation and rotation to the overall amplitude of the displacement field.

Both $\boldsymbol{A}$ and $\boldsymbol{B}$ are diagonal, indicating that SOI terms do not include interactions between $|u\rangle$ and $|\theta\rangle$. Thus, we can consider these terms as effective forces and moments that act on translation and rotation, respectively. For instance, $\boldsymbol{B}\otimes\hat{\boldsymbol{S}}_3\hat{p}_\eta|\psi\rangle$ contains the equivalent force and moment acting on $|u\rangle$ and

$|\theta\rangle$, which are $|F\rangle_{S_3} = -2\tau\alpha_s\hat{\boldsymbol{S}}_3\hat{p}_\eta\,|u\rangle$ and $|M\rangle_{S_3} = -2\tau\beta_f\hat{\boldsymbol{S}}_3\hat{p}_\eta\,|\theta\rangle$, respectively. Taking $|F\rangle_{S_3}$ as an example, its vector form in the local coordinate system can be represented as $-2i\tau\alpha_s k_\eta(u_2\boldsymbol{e}_1 - u_1\boldsymbol{e}_2) = -\frac{2\tau\alpha_s k_\eta}{\omega}\boldsymbol{e}_3 \times \partial_t\boldsymbol{u}$, which is perpendicular to both axis $\boldsymbol{e}_3$ and velocity $\partial_t\boldsymbol{u} = -i\omega u_j\boldsymbol{e}_j$. Consequently, the synthetic gauge potential can be considered as the "Coriolis" term resulting from rotation around the $\boldsymbol{e}_3$-axis, with its sign depends on k_η. Similar understanding can be applied to other terms that involve the products of $\hat{\boldsymbol{S}}_j$ and k_η. These terms will result into circular polarized modes with k_η-dependent chirality.

Data, Materials, and Software Availability. The data supporting the conclusions of this study are included within the paper text, figures, and *SI Appendix*. Additional data and codes are available at Zenodo (DOI: https://doi.org/10.5281/zenodo.13978821) (53).

ACKNOWLEDGMENTS. We acknowledge the support from the National Natural Science Foundation of China (No. 11935010), the National Key R&D Program of China (No. 2023YFA1406900 and No. 2022YFA1404400), the Natural Science Foundation of Shanghai (No. 23ZR1481200), the Program of Shanghai Academic Research Leader (No. 23XD1423800), and the Opening Project of Shanghai Key Laboratory of Special Artificial Microstructure Materials and Technology.

Author affiliations: [a]Center for Phononics and Thermal Energy Science, China-EU Joint Lab on Nanophononics, Shanghai Key Laboratory of Special Artificial Microstructure Materials and Technology, School of Physics Science and Engineering, Tongji University, Shanghai 200092, China

1. J. H. Poynting, The wave motion of a revolving shaft, and a suggestion as to the angular momentum in a beam of circularly polarised light. *Proc. R. Soc. Lond. Ser. A* **82**, 560–567 (1909).
2. V. S. Liberman, B. Y. Zel'dovich, Spin-orbit interaction of a photon in an inhomogeneous medium. *Phys. Rev. A* **46**, 5199–5207 (1992).
3. K. Y. Bliokh, F. J. Rodríguez-Fortuño, F. Nori, A. V. Zayats, Spin-orbit interactions of light. *Nat. Photon.* **9**, 796–808 (2015).
4. J. Wunderlich, B. Kaestner, J. Sinova, T. Jungwirth, Experimental observation of the spin-hall effect in a two-dimensional spin-orbit coupled semiconductor system. *Phys. Rev. Lett.* **94**, 047204 (2005).
5. K. Y. Bliokh, Y. P. Bliokh, Conservation of angular momentum, transverse shift, and spin hall effect in reflection and refraction of an electromagnetic wave packet. *Phys. Rev. Lett.* **96**, 073903 (2006).
6. X. Yin, Z. Ye, J. Rho, Y. Wang, X. Zhang, Photonic spin hall effect at metasurfaces. *Science* **339**, 1405–1407 (2013).
7. O. Hosten, P. Kwiat, Observation of the spin hall effect of light via weak measurements. *Science* **319**, 787–790 (2008).
8. K. Y. Bliokh, F. Nori, Transverse spin of a surface polariton. *Phys. Rev. A* **85**, 061801 (2012).
9. S. Y. Lee *et al*., Role of magnetic induction currents in nanoslit excitation of surface plasmon polaritons. *Phys. Rev. Lett.* **108**, 213907 (2012).
10. J. Lin *et al*., Polarization-controlled tunable directional coupling of surface plasmon polaritons. *Science* **340**, 331–334 (2013).
11. L. Huang *et al*., Helicity dependent directional surface plasmon polariton excitation using a metasurface with interfacial phase discontinuity. *Light Sci. Appl.* **2**, e70–e70 (2013).
12. T. Van Mechelen, Z. Jacob, Universal spin-momentum locking of evanescent waves. *Optica* **3**, 118–126 (2016).
13. X. Zhou, Z. Xiao, H. Luo, S. Wen, Experimental observation of the spin hall effect of light on a nanometal film via weak measurements. *Phys. Rev. A* **85**, 043809 (2012).
14. L. Ahlawat, K. Kishor, R. K. Sinha, Photonic spin hall effect-based ultra-sensitive refractive index sensor for haemoglobin sensing applications. *Opt. Laser Technol.* **170**, 110183 (2024).
15. F. J. Rodriguez-Fortu *et al*., Near-field interference for the unidirectional excitation of electromagnetic guided modes. *Science* **340**, 328–330 (2013).
16. J. Petersen, J. Volz, A. Rauschenbeutel, Chiral nanophotonic waveguide interface based on spin-orbit interaction of light. *Science* **346**, 67–71 (2014).
17. D. O'Connor, P. Ginzburg, F. J. Rodríguez-Fortuño, G. A. Wurtz, A. V. Zayats, Spin-orbit coupling in surface plasmon scattering by nanostructures. *Nat. Commun.* **5**, 5327 (2014).
18. Z. Shao, J. Zhu, Y. Chen, Y. Zhang, S. Yu, Spin-orbit interaction of light induced by transverse spin angular momentum engineering. *Nat. Commun.* **9**, 926 (2018).
19. Y. Long, J. Ren, H. Chen, Intrinsic spin of elastic waves. *Proc. Natl. Acad. Sci. U.S.A.* **115**, 9951 (2018).
20. G. J. Chaplain, J. M. De Ponti, R. V. Craster, Elastic orbital angular momentum. *Phys. Rev. Lett.* **128**, 064301 (2022).
21. K. Y. Bliokh, Elastic spin and orbital angular momenta. *Phys. Rev. Lett.* **129**, 204303 (2022).
22. J. Ren, From elastic spin to phonon spin: Symmetry and fundamental relations. *Chin. Phys. Lett.* **39**, 126301 (2022).
23. W. Fu *et al*., Phononic integrated circuitry and spin-orbit interaction of phonons. *Nat. Commun.* **10**, 2743 (2019).
24. Z. Feng, Y. Liu, X. Xi, L. Wang, X. Sun, Gigahertz phononic integrated circuits based on overlay slot waveguides. *Phys. Rev. Appl.* **19**, 064076 (2023).
25. W. Yuan *et al*., Observation of elastic spin with chiral meta-sources. *Nat. Commun.* **12**, 6954 (2021).
26. L. Cao, S. Wan, Y. Zeng, Y. Zhu, B. Assouar, Observation of phononic skyrmions based on hybrid spin of elastic waves. *Sci. Adv.* **9**, eadf3652 (2023).
27. W. H. Wittrick, On elastic wave propagation in helical springs. *Int. J. Mech. Sci.* **8**, 25–47 (1966).
28. G. Eason, Wave propagation in a naturally curved elastic rod. *J. Sound Vibration* **36**, 491–511 (1974).
29. B. Tabarrok, Y. Xiong, On the buckling equations for spatial rods. *Int. J. Mech. Sci.* **31**, 179–192 (1989).
30. L. E. Becker, W. L. Cleghorn, On the buckling of helical compression springs. *Int. J. Mech. Sci.* **34**, 275–282 (1992).
31. J. Boulanger, N. Le Bihan, S. Catheline, V. Rossetto, Observation of a non-adiabatic geometric phase for elastic waves. *Ann. Phys.* **327**, 952–958 (2012).
32. J. A. Iglesias Martínez *et al*., Experimental observation of roton-like dispersion relations in metamaterials. *Sci. Adv.* **7**, eabm2189 (2021).
33. J. Kishine, A. S. Ovchinnikov, A. A. Tereshchenko, Chirality-induced phonon dispersion in a noncentrosymmetric micropolar crystal. *Phys. Rev. Lett.* **125**, 245302 (2020).
34. S. Wang, G. Ma, C. T. Chan, Topological transport of sound mediated by spin-redirection geometric phase. *Sci. Adv.* **4**, eaaq1475 (2018).
35. C. N. Alexeyev, M. A. Yavorsky, Topological phase evolving from the orbital angular momentum of 'coiled' quantum vortices. *J. Opt. A Pure Appl. Opt.* **8**, 752 (2006).
36. K. Y. Bliokh, Geometrical optics of beams with vortices: Berry phase and orbital angular momentum hall effect. *Phys. Rev. Lett.* **97**, 043901 (2006).
37. Y. Zhang *et al*., Elastic wave spin and unidirectional routing in thin rod systems. *Int. J. Mech. Sci.* **277**, 109512 (2024).
38. T. Frenzel, J. Köpfler, E. Jung, M. Kadic, M. Wegener, Ultrasound experiments on acoustical activity in chiral mechanical metamaterials. *Nat. Commun.* **10**, 3384 (2019).
39. Q. Tong, J. Li, S. Wang, Acoustic circular dichroism in a three-dimensional chiral metamaterial. *Phys. Rev. B* **107**, 134103 (2023).
40. B. Auld, *Acoustic Fields and Waves in Solids* (Wiley, 1973).
41. M. Lanoy, F. Lemoult, A. Eddi, C. Prada, Dirac cones and chiral selection of elastic waves in a soft strip. *Proc. Natl. Acad. Sci. U.S.A.* **117**, 30186 (2020).
42. C. Yang *et al*., Hybrid spin and anomalous spin-momentum locking in surface elastic waves. *Phys. Rev. Lett.* **131**, 136102 (2023).
43. S. H. Mousavi, A. B. Khanikaev, Z. Wang, Topologically protected elastic waves in phononic metamaterials. *Nat. Commun.* **6**, 8682 (2015).
44. M. Yan *et al*., On-chip valley topological materials for elastic wave manipulation. *Nat. Mater.* **17**, 993–998 (2018).
45. S. Y. Yu *et al*., Elastic pseudospin transport for integratable topological phononic circuits. *Nat. Commun.* **9**, 3072 (2018).
46. J. Zhao *et al*., Elastic valley spin controlled chiral coupling in topological valley phononic crystals. *Phys. Rev. Lett.* **129**, 275501 (2022).
47. Y. Huang *et al*., Parity-frequency-space elastic spin control of wave routing in topological phononic circuits. *Adv. Sci.* **11**, e2404839 (2024).
48. A. D. O'Connell *et al*., Quantum ground state and single-phonon control of a mechanical resonator. *Nature* **464**, 697–703 (2010).
49. A. Zivari, R. Stockill, N. Fiaschi, S. Gröblacher, Non-classical mechanical states guided in a phononic waveguide. *Nat. Phys.* **18**, 789–793 (2022).
50. M. Weiler *et al*., Elastically driven ferromagnetic resonance in nickel thin films. *Phys. Rev. Lett.* **106**, 117601 (2011).
51. X. Zhang, G. E. W. Bauer, T. Yu, Unidirectional pumping of phonons by magnetization dynamics. *Phys. Rev. Lett.* **125**, 077203 (2020).
52. T. Sato, W. Yu, S. Streib, G. E. W. Bauer, Dynamic magnetoelastic boundary conditions and the pumping of phonons. *Phys. Rev. B* **104**, 014403 (2021).
53. C. Yang, File for Chirality-induced Phonon Spin Selectivity by Elastic Spin–orbit Interaction. Zenodo. 10.5281/zenodo.13978821. Deposited 23 October 2024.